nature communications

Article

https://doi.org/10.1038/s41467-024-53941-8

Electron transfer mediated activation of periodate by contaminants to generate $^1O_2$ by charge-confined single-atom catalyst

Received: 2 July 2024

Accepted: 29 October 2024

Published online: 05 November 2024

Check for updates

Qianqian Tang[1], Bangxiang Wu[1], Xiaowen Huang[1], Wei Ren[1], Lingling Liu[1,2], Lei Tian[1], Ying Chen[1], Long-Shuai Zhang[1,2] ✉, Qing Sun[1,2], Zhibing Kang[1], Tianyi Ma[3] & Jian-Ping Zou[1,2] ✉

The electron transfer process (ETP) is able to avoid the redox cycling of catalysts by capturing electrons from contaminants directly. However, the ETP usually leads to the formation of oligomers and the reduction of oxidants to anions. Herein, the charge-confined Fe single-atom catalyst (Fe/SCN) with Fe-N_3S_1 configuration was designed to achieve ETP-mediated contaminant activation of the oxidant by limiting the number of electrons gained by the oxidant to generate $^1O_2$. The Fe/SCN-activate periodate (PI) system shows excellent contaminant degradation performance due to the combination of ETP and $^1O_2$. Experiments and DFT calculations show that the Fe/SCN-PI* complex with strong oxidizing ability triggers the ETP, while the charge-confined effect allows the single-electronic activation of PI to generate $^1O_2$. In the Fe/SCN + PI system, the 100% selectivity dechlorination of ETP and the ring-opening of $^1O_2$ avoid the generation of oligomers and realize the transformation of large-molecule contaminants into small-molecule biodegradable products. Furthermore, the Fe/SCN + PI system shows excellent anti-interference ability and application potential. This work pioneers the generation of active species using ETP's electron to activate oxidants, which provides a perspective on the design of single-atom catalysts via the charge-confined effect.

Advanced oxidation processes (AOPs) have been widely used for contaminants disposal driven by their high efficiency and strong oxidation capacity[1–3]. In conventional AOPs, an oxidant is activated by one electron from the catalyst to generate strongly oxidizing active species for the degradation of contaminants[4,5]. Although the activation process of oxidants by catalysts significantly improves the degradation of contaminants, the difficult redox cycling of the active sites of catalysts makes the catalysts-activated AOPs suffer from the consumption of catalysts and the low utilization of oxidants[6–8]. In addition, the indiscriminate attack of strongly oxidizing active species makes them susceptible to interference from various impurities in the actual water body, thus making it challenging to achieve targeted degradation of contaminants[9,10].

Recently, the ETP has been found to degrade contaminants via catalyst-mediated electron transfer from contaminants to oxidants, showing the characteristics of the non-radical pathway with the efficient utilization of oxidants and the avoidance of the redox cycling of catalysts[11–13]. Unfortunately, the absence of active species in the ETP system enables the contaminants that have lost electrons to polymerize with each other to form oligomers and occupy the active sites on the catalyst[14,15]. In this way, the catalyst still exhibits poor reusability. However, the deep treatment of contaminants is habitually overlooked

[1]Key Laboratory of Jiangxi Province for Persistent Pollutants Prevention Control and Resource Reuse, Nanchang Hangkong University, Nanchang 330063, P. R. China. [2]National-Local Joint Engineering Research Center of Heavy Metals Pollutants Control and Resource Utilization, Nanchang Hangkong University, Nanchang 330063, P. R. China. [3]School of Science, RMIT University, Melbourne VIC 3000, Australia. ✉e-mail: L_S_Zhang1990@163.com; zjp_112@126.com

in the ETP systems, and current endeavors are mostly focused on the use of catalysts with excellent conductivity to mediate the electron transfer between reactants[16,17]. Based on the uneven dispersion of active sites as well as the excellent conductivity of the catalyst, the unlimited transfer of electrons induces the oxidants (PI and persulfate, etc.) in the ETP system to get two electrons to be directly reduced to anions, resulting in the absence of active species[18–20]. If the oxidant obtains only one electron from contaminants via the ETP, the active species will be generated. Meanwhile, the advantages of catalytic-activated AOPs and ETP will be combined in a single system. Therefore, it is necessary to design catalysts that can control the number of electrons transferred from contaminants to oxidants.

Heptazine-based carbon nitride (C_3N_4) forms a C-N conjugated framework due to the sp^2 hybridized π-conjugated structure within the heptazine unit. Whereas, the bridged N atoms are sp^3-hybridized and are unable to form a conjugation together with the heptazine ring[21,22]. Consequently, C_3N_4 can confine the charge within each heptazine unit, which is an ideal candidate for controlling the number of transferred electrons[23]. However, the lack of adsorption sites for reactants makes it difficult to induce the ETP reaction[24,25]. The dual-site catalysts have been validated to enable the adsorption of different reactants[26,27]. Compared with the dual metal sites, the metal-nonmetal dual-site catalysts can provide active sites for C_3N_4 without changing the charge-confined properties. Especially, the noncovalent interactions between chalcogen elements (i.e., S···O) provide a robust basis for appropriate interactions between nonmetal sites and reactants[28,29]. In addition, the coordination between nonmetal and metal single atoms is able to serve as a channel for rapid and directional charge transfer[24,30]. Hence, the single atom catalyst supported by nonmetal-doped C_3N_4 will achieve electron transfer mediated the activation of oxidants by contaminant to generate active species via charge confinement.

In this work, the S-doped C_3N_4-loaded Fe single-atom catalyst (Fe/SCN) has been successfully prepared. The atomic level distribution of Fe and the coordination configuration of the active site as Fe-N_3S_1 are confirmed. The Fe/SCN + PI system exhibits excellent degradation performance for 4-Chlorophenol (4-CP) via the synergistic mechanism of ETP and $^1O_2$. Furthermore, it does confirm that $^1O_2$ is derived from the activation of PI by electrons conducted from contaminants rather than the activation of PI by the Fe/SCN itself. DFT calculations verify that the charge channel of the Fe-S bond and the charge-confined active site enables electrons from 4-CP to be transferred to PI via a single-electron pathway, resulting in the generation of $^1O_2$. The dechlorination of 4-CP is accomplished by the ETP in the Fe/SCN + PI system, while the ring-opening of the intermediates is further achieved by the $^1O_2$ generated from the contaminants-activated PI, thus avoiding the generation of oligomeric products. This study proposes the concept of the charge-confined single-atom catalyst and applies it to the rational design of the Fe/SCN, which realizes the activation of PI by the electron from the contaminant to generate $^1O_2$ via the ETP system.

Results

Characterization of catalysts

The Fe/SCN was synthesized according to our previous work with a slight modification[31]. The X-ray diffraction (XRD) patterns and Fourier-transform infrared spectroscopy (FTIR) spectra indicate that the Fe/SCN possesses a graphitic carbon nitride texture, and no Fe nanoparticles or iron sulfides are detected (Supplementary Fig. 1). Additionally, the Fe/SCN exhibits a lamellar morphology without visible Fe nanoparticles (Fig. 1a, b), indicating the excellent dispersion of Fe. As shown in Fig. 1c and Supplementary Fig. 2, the tiny bright spots in the aberration-corrected high-angle annular dark-field scanning transmission electron microscopy (AC-HAADF-STEM) images of different regions prove the atomic dispersion of Fe atoms in the Fe/SCN[32]. Energy-dispersive X-ray (EDX) elemental mapping images (Fig. 1d) demonstrate that Fe and S are evenly distributed in the Fe/SCN. The precise Fe content is confirmed to be 6.20 wt% by inductively coupled plasma-optical emission spectrometry (ICP-OES). The specific surface area of the Fe/SCN (76.194 $m^2 g^{-1}$) is larger than that of CN, SCN, and Fe/CN (Supplementary Fig. 3 and Table 1), which can provide more active sites for catalytic reactions[33].

X-ray adsorption was employed to explore the chemical state and coordination environment of the Fe atoms in the Fe/SCN. The Fe K-edge X-ray absorption near edge structure (XANES) spectrum of the Fe/SCN is located between that of FeO and Fe_2O_3 (Fig. 1e), indicating that the oxidation state of Fe in the Fe/SCN is between +2 and +3[34]. As shown in Fig. 1f, the Fourier transform extended X-ray absorption fine structure (FT-EXAFS) spectrum of the Fe/SCN has only one dominant peak located at 1.53 Å. The peaks of Fe-Fe (2.21 Å) and Fe-O (2.67 Å) are not detected, consistent with the wavelet transform images (Supplementary Fig. 4), showing that the Fe in the Fe/SCN is atomically dispersed[31]. The maximum peak of the Fe/SCN displays a slight positive shift than that of the FePc (Fig. 1f and Supplementary Fig. 4), showing that the atoms coordinated with Fe in the Fe/SCN are heteroatoms with a larger atomic radius than N[35]. Additionally, the Fe-N and Fe-S peaks, which are not present in SCN, are detected in the N *1 s* and S *2p* spectra of the Fe/SCN, respectively, indicating that both S and N are coordination atoms of Fe (Supplementary Figs. 5 and 6)[36–38]. The EXAFS-fitting results (Fig. 1g and Supplementary Table 2) show that the average coordination numbers of Fe-N and Fe-S are 3.3 and 0.9, respectively. From the above results, it is worth noting that the isolated Fe atom in the Fe/SCN is coordinated with three N atoms and one S atom to form the Fe-N_3S_1 moiety.

Periodate activation by Fe/SCN

The catalytic activities of the as-prepared samples were evaluated by activating PI to degrade 4-CP. As shown in Fig. 2a, the adsorption performances of the as-prepared catalysts for 4-CP are weak, and all of them are less than 5%. When the PI is added, neither CN nor SCN can degrade 4-CP, indicating that they cannot activate PI. The homogeneous Fe^{2+} or Fe^{3+} also have no performance on degrading 4-CP (Supplementary Fig. 7), whereas the Fe/CN has a rapid 4-CP degradation ability, demonstrating that the anchored Fe single atom is the active site for activating PI. Furthermore, the complete inhibition in the degradation performance of the Fe/CN + PI system by the incorporation of KSCN as a masking agent for Fe sites further confirms the importance of Fe sites in heterogeneous catalysts for the activation of the PI (Supplementary Fig. 8). Using the Fe/SCN to activate PI, the degradation rate of 4-CP is further improved. The optimization apparent reaction rate constant (k_{obs}, min^{-1}) for the Fe/SCN (0.189 min^{-1}) to decompose 4-CP is 2.3-fold higher than that of the Fe/CN (Supplementary Figs. 9–13), indicating that the Fe and S have a synergistic enhancement effect on the activation of PI.

To explore the reactive species, quenching experiments and electron paramagnetic resonance (EPR) tests were conducted. Tert-butanol (TBA), p-benzoquinone (p-BQ), furfuryl alcohol (FFA), and potassium dichromate ($K_2Cr_2O_7$) were used as scavengers of ·OH, $\cdot O_2^-$, $^1O_2$, and e^-, respectively[39,40]. For the Fe/CN + PI system, the active species of ·OH, $\cdot O_2^-$, and $^1O_2$ are verified by quenching experiments and EPR (Fig. 2b and Supplementary Fig. 14). Moreover, the ETP and Fe(IV) species are not detected (Fig. 2b and Supplementary Fig. 15). Hence, the degradation of 4-CP by Fe/CN-activated PI is a process accomplished synergistically by radicals and nonradicals. As demonstrated in Fig. 2b, the TBA does not affect the degradation rate of 4-CP, showing that there is no ·OH in the Fe/SCN + PI system. As shown in Fig. 2c, the DMPO-·O_2^- and TEMP-$^1O_2$ adducts are detected, consistent with the results of the quenching experiments (Fig. 2b), confirming the generation of $\cdot O_2^-$ and $^1O_2$ in the Fe/SCN + PI system. As shown in Fig. 2d, the superoxide dismutase (SOD) can completely inhibit the generation of $^1O_2$, suggesting that all of the $^1O_2$ in the Fe/SCN + PI system are

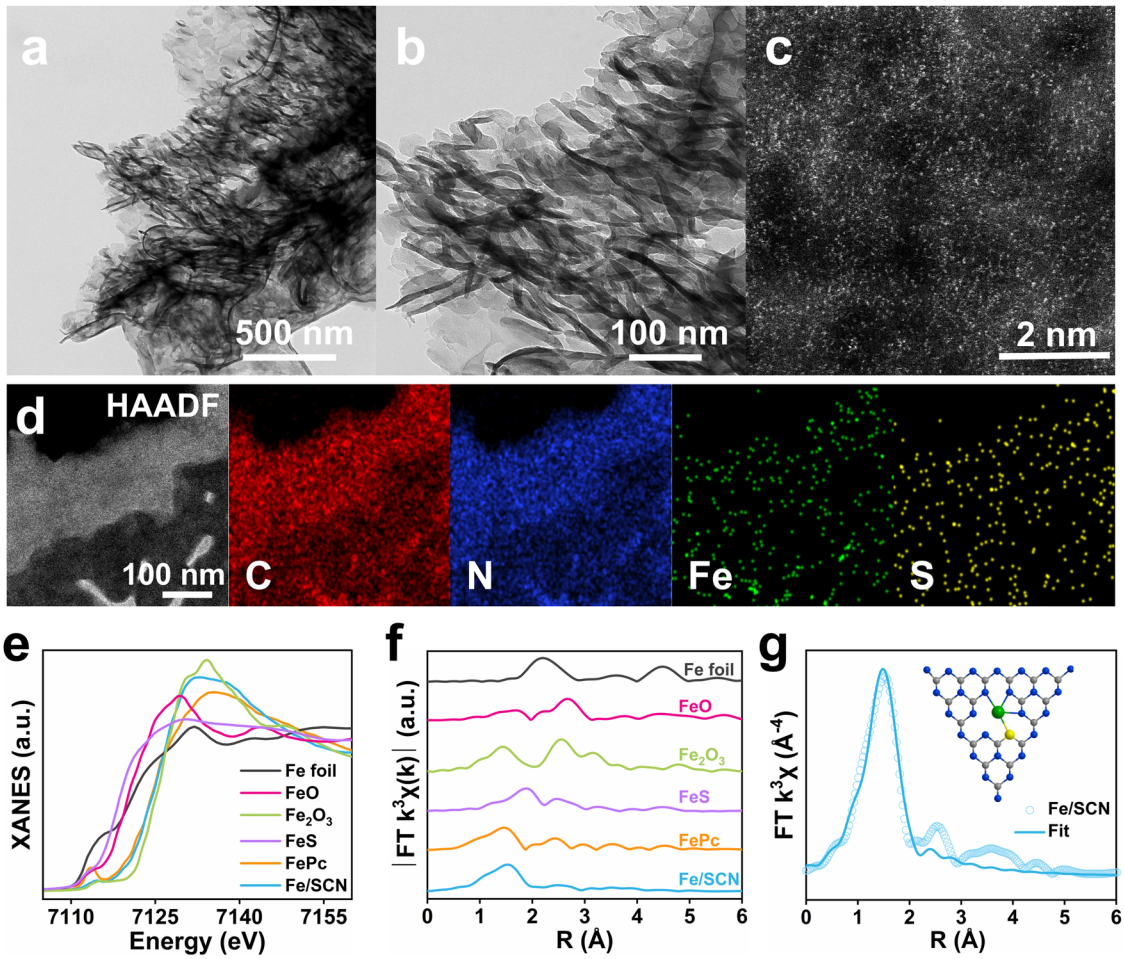

Fig. 1 | Characterization of Fe/SCN. a–d TEM (**a**, **b**), AC-HAADF-STEM (**c**), and elemental mapping (**d**) images of the Fe/SCN. **e**, **f** Fe K-edge XANES (**e**) and k^3-weighted fourier transform (**f**) spectra of the Fe/SCN and reference samples. **g** EXAFS fitting curve in R space of the Fe/SCN (inset: structural model of the Fe/SCN, Fe: green, S: yellow, N: blue, C: grey).

generated by the intermediate $\cdot O_2^-$ (Eqs. (1–2))[41,42]. The discordant inhibition effects of p-BQ and FFA in the Fe/SCN + PI system can be attributed to the electron-donating effect of FFA, which allows the FFA to replace 4-CP to complete the electron-donating process in order to cause excessive inhibition effects (Supplementary Fig. 16)[43]. The presence of ETP in the Fe/SCN + PI system was further investigated. For the Fe/SCN + PI system, quenching electrons can significantly inhibit the degradation of 4-CP, tentatively suggesting that ETP plays a role in the degradation of 4-CP (Fig. 2b). As shown in Fig. 2e, the characteristic peaks of DMPOX, which was generated by the non-radical mediated oxidation of DMPO, is also a side evidence of the presence of ETP in the Fe/SCN + PI system[19]. Compared with the Fe/CN + PI system, the Fe/SCN + PI system has lower oxidant consumption in the case of degrading the same amount of 4-CP (Supplementary Fig. 17), which is one of the characteristics of the ETP system[44]. Additionally, the removal of 4-CP and the consumption of PI have a very good linear correlation (Fig. 2f), indicating that the decomposition of 4-CP and PI simultaneously occurs[19]. As shown in Fig. 2g, the Fe/SCN displays an obvious change in current response when PI and 4-CP are added successively, corresponding to the formation of the catalyst-PI* complexes and the trigger of the ETP reaction, respectively[14,45]. Correspondingly, the increase in potential after adding PI proves that the formed catalyst-PI* complexes induce a higher redox potential (Fig. 2h), which can facilitate the subsequent oxidation of contaminants[46]. A more significant decrease in potential is observed at the Fe/SCN compared to the Fe/CN after the addition of 4-CP, confirming that the catalyst-PI* complex is directly consumed by 4-CP[47]. The results of the oxidant consumption test and electrochemical experiments fully prove the existence of the ETP in the Fe/SCN + PI system. In conclusion, both $^1O_2$ and ETP act on the degradation of 4-CP in the Fe/SCN + PI system.

$$3IO_4^- + 2OH^- \rightarrow 3IO_3^- + 2 \cdot O_2^- + H_2O \quad (1)$$

$$IO_4^- + 2 \cdot O_2^- + H_2O \rightarrow IO_3^- + 2OH^- + 2^1O_2 \quad (2)$$

Mechanism investigation of Fe/SCN+PI system

The relationship between $^1O_2$ and ETP in the Fe/SCN + PI system is further explored. In Fig. 3a, different atmospheres (Air, O_2, and Ar) do not affect the catalytic performance of the Fe/SCN + PI system, showing that the reactive oxygen species are all from PI and are not related to dissolved oxygen[31]. Moreover, the concentration of PI in the Fe/SCN + PI system remains unchanged for 30 min before the addition of 4-CP, while decreases over time after the addition of 4-CP (Supplementary Fig. 18), indicating that 4-CP is the initiator of the Fe/SCN + PI system[43]. The EPR signal of $\cdot O_2^-$ increases obviously after the addition of 4-CP (Supplementary Fig. 19), verifying that the electrons provided by 4-CP promote the generation of reactive oxygen species[30]. As depicted in Fig. 3b, the $K_2Cr_2O_7$ greatly suppresses the signal intensity of $^1O_2$. Moreover, the fluorescence signal of 9,10-dimethylanthracene

https://doi.org/10.1038/s41467-024-53941-8

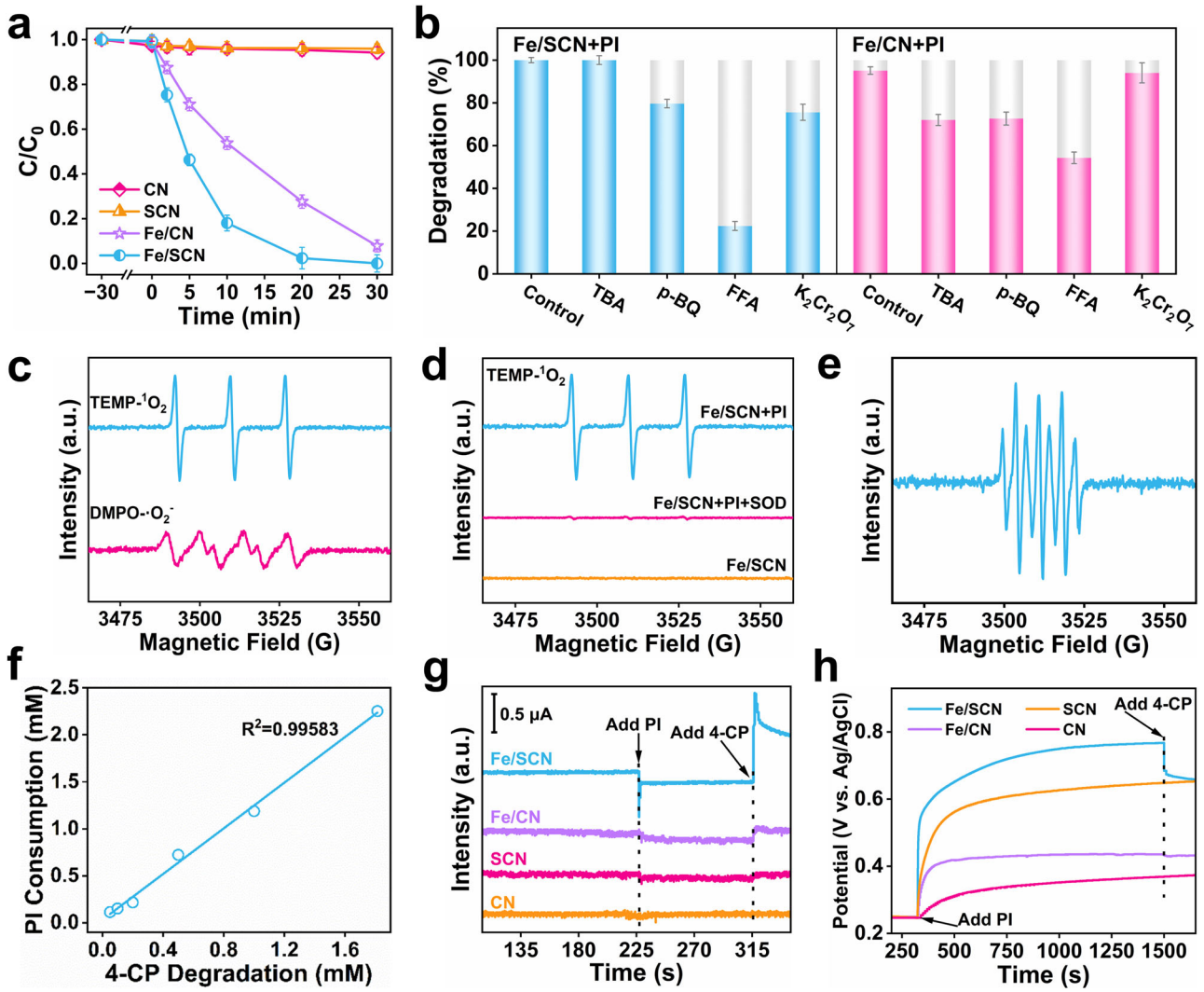

Fig. 2 | Performance of contaminant removal and analysis of active species. **a** 4-CP degradation curves of different samples. **b**, Quenching experiments of the Fe/CN + PI and the Fe/SCN + PI systems (the error bars in **a** and **b** are all standard deviations calculated from the results of three parallel experiments). **c** EPR signals of $^1O_2$ and $\cdot O_2^-$ in the Fe/SCN + PI system. **d** EPR signals of $^1O_2$ in different system. **e** EPR spectrum of DMPO adducts in the Fe/SCN + PI system. **f** Correlation between 4-CP degradation and PI consumption in the Fe/SCN + PI system. **g**, **h** Chronoamperometry (**g**) and chronopotentiometry (**h**) curves of different catalysts.

(DMA, a classical chemical probe that can react with $^1O_2$ to form DMA-O_2) decreases significantly only after the addition of 4-CP as the electron donor (Fig. 3c, d)[48]. All of the above results demonstrate that the Fe/SCN + PI system is triggered by ETP, and then the electron from 4-CP activates PI to generate $^1O_2$.

In order to figure out the electron transfer route in the Fe/SCN system, the adsorption sites of the reactants on the Fe/SCN surface are explored. As shown in Fig. 2h, the open-circuit potential of the SCN after the addition of PI is higher than that of the Fe/CN and CN. The more significant potential increase after introduction of the S-site confirms the successful realization of the design idea of introducing the S-site as the adsorption site of PI. As illustrated in the high-resolution I *3d* XPS spectra (Supplementary Fig. 20), neither the CN nor the Fe/CN possess the adsorption capacity of PI, while the SCN and Fe/SCN exhibit obvious peaks of I *3d*, revealing that the S site is essential for the interaction between the Fe/SCN and PI. When 4-CP and PI simultaneously exist, a comparison is made between the energies of the Fe and S dual sites for different modes of co-adsorption of the reactants (Fig. 3e). In comparison, the co-adsorption model, in which 4-CP interacts with the Fe site at the Cl-terminus and the PI adsorbs at the S site, has a much lower energy than the other model, which is consistent with the above XPS results. This provides the underlying conditions for the rapid transfer of electrons from 4-CP to PI via the Fe-S transport channel. As demonstrated in Fig. 3f, a large number of electrons are enriched at the PI molecule after the co-adsorption of 4-CP and PI. The number of charges received by the PI molecule is 0.88 e as evidenced by Bader charge calculations. The differential charge density analysis of the Fe/SCN reveals that the conjugate distribution of charges inside the heptazine ring enables electrons to move inside the heptazine ring easily (Fig. 3g), whereas it is difficult for the electrons to cross over and undergo long-range transfer between heptazine rings. Thus, the reactions of each Fe-N_3S_1 active moiety do not interfere with each other due to the unique charge-confined nature of heptazine units. In addition, it is clarified by the rotating ring-disk electrode test that the electron transfer number during the degradation of 4-CP by the Fe/SCN + PI system converges to 1 (Fig. 3h), causing the generation of reactive oxygen species from the activated PI via single-electron transfer. In conclusion, the Fe/SCN achieved the activation of PI by the electron from contaminants to generate $^1O_2$ via the single-electron transfer.

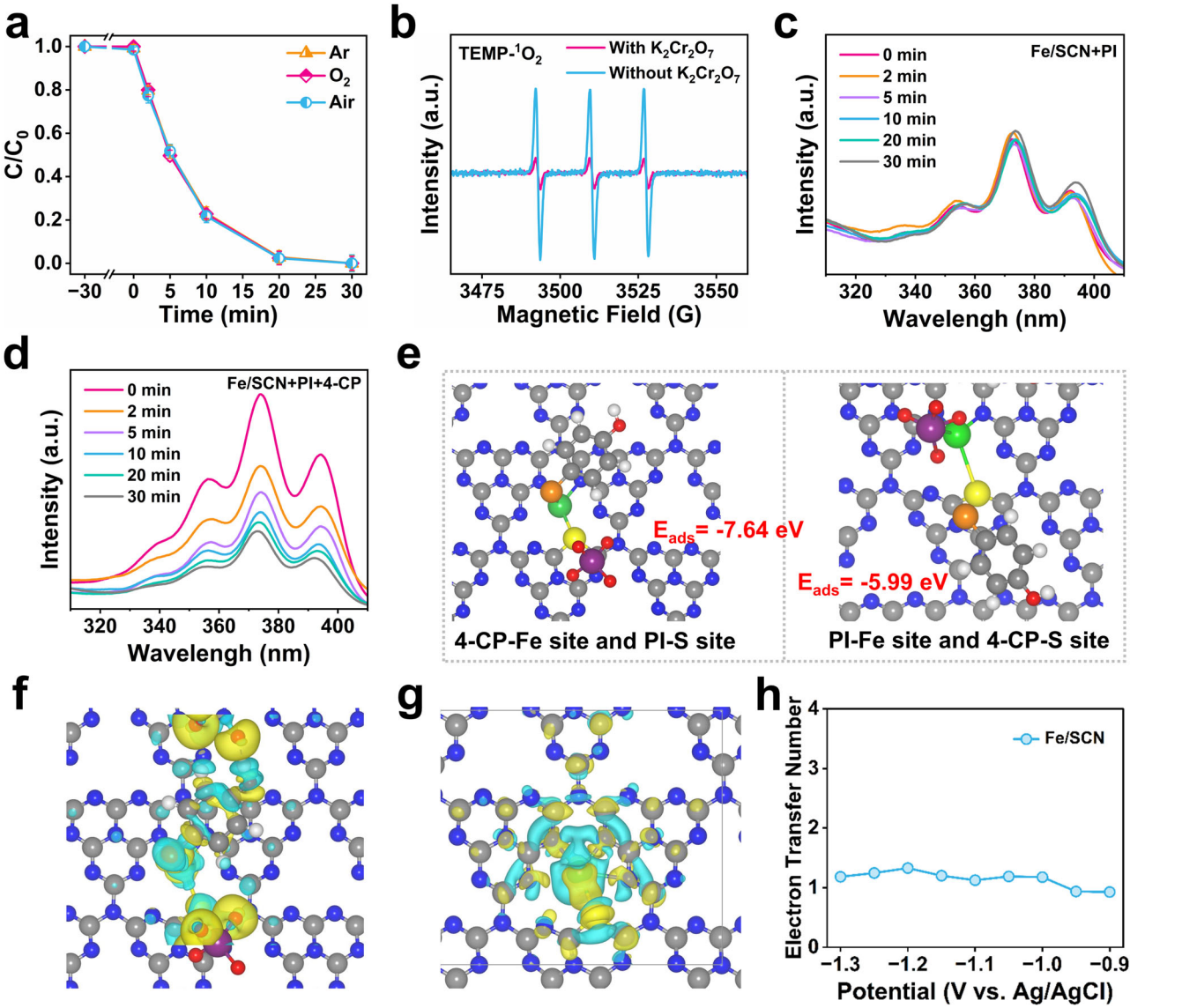

Fig. 3 | Mechanism analysis of Fe/SCN + PI system by theoretical and experimental. a 4-CP degradation curves of the Fe/SCN + PI system under different atmospheres (the error bars are all standard deviations calculated from the results of three parallel experiments). **b** EPR signals of $^1O_2$ in the Fe/SCN + PI system with and without $K_2Cr_2O_7$, respectively. **c**, **d** Photoluminescence of DMA in Fe/SCN + PI (**c**) and Fe/SCN + PI + 4-CP (**d**) systems. **e** The comparison of the energies of the Fe and S dual sites for different modes of co-adsorption of the reactants (Fe: green, S: yellow, N: blue, C: grey, O: red, Cl: orange, H: white, I: purple). **f** Charge density difference of Fe-N_3S_1 sites after 4-CP and PI co-adsorption. **g** Charge density difference diagram for the Fe/SCN (The cyan and light yellow iso-surfaces depict electron depletion and accumulation, respectively). **h** The electron transfer numbers of the Fe/SCN + PI system.

Contaminant degradation pathways

After figuring out the electron transfer process and PI activation mechanism in the Fe/SCN + PI system, the degradation pathway of this system towards 4-CP is further explored. As illustrated in Fig. 4a, when the degradation ratio of 4-CP is 92%, the dechlorination ratio is only 31% in the Fe/CN + PI system, whereas the Fe/SCN + PI system achieves 100% dechlorination of 4-CP. In addition, the change in PI concentration before and after the addition of 4-CP indicates that the Fe/SCN + PI system is triggered by ETP (Supplementary Fig. 18). The DFT calculations prove that 4-CP is adsorbed on the Fe site of the Fe/SCN by the terminal Cl (Fig. 3e). Hence, the degradation of 4-CP in the Fe/SCN + PI system originates from dechlorination induced by ETP. When the p-benzoquinone (the product obtained after 4-CP dechlorination) is used as the target contaminant in the Fe/SCN + PI system, the p-benzoquinone and PI concentrations show no obvious change (Fig. 4b). The results indicate that the ETP only accomplished the dechlorination of 4-CP without further degradation. Unlike traditional ETP, oligomers are easily produced after dechlorination, while no oligomers are detected in the Fe/SCN + PI system (Fig. 4c). As can be seen from Fig. 4d and Supplementary Fig. 21, the concentration of macromolecule products ($C_6H_6O_2$ and $C_6H_4O_2$) shows a trend of increase and then a decrease, while the concentration of micromolecule products ($C_4H_4O_4$, $C_3H_4O_2$, and $C_2H_4O_3$) continues to increase, suggesting that 4-CP is gradually converted into the small-molecule products after dechlorination in the presence of $^1O_2$, an active species with good ring-opening properties[49]. The total organic carbon (TOC) test results also demonstrate that the Fe/SCN + PI system can degrade the macromolecule organic pollutants to micromolecule products (Supplementary Fig. 22). The degradation pathway of 4-CP by the Fe/SCN + PI system is summarized (Fig. 4e). Firstly, the Cl of 4-CP is removed by ETP to produce p-benzoquinone, while the electrons from the ETP activate PI to produce $^1O_2$. Then, the p-benzoquinone is further ring-opened by $^1O_2$ to generate micromolecular products. Advantageously, the continuous generation of

https://doi.org/10.1038/s41467-024-53941-8

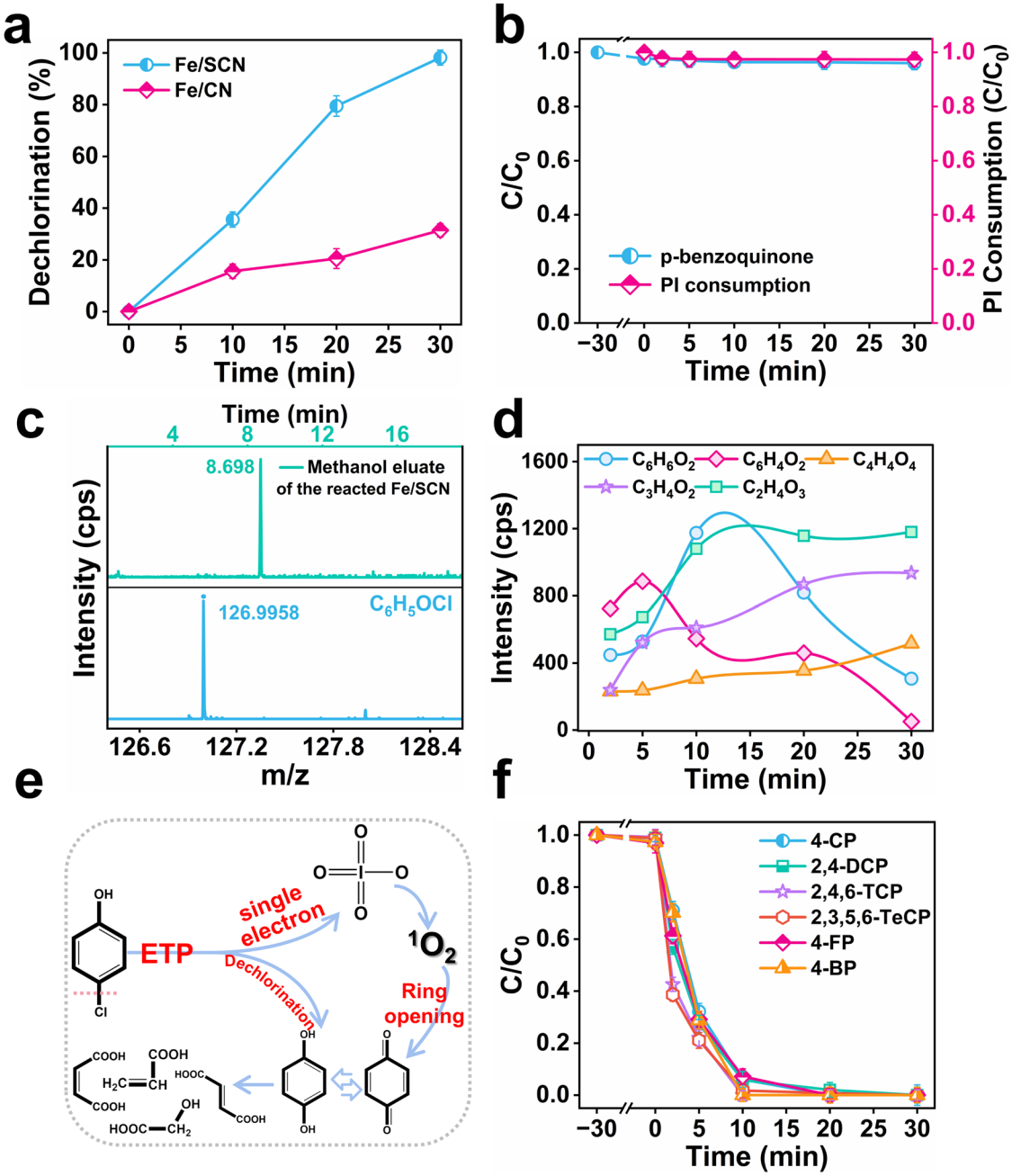

Fig. 4 | Exploration of contaminant degradation pathways. a Dechlorination rate of 4-CP by the Fe/CN + PI and the Fe/SCN + PI systems. **b** Degradation curve of p-benzoquinone in the Fe/SCN + PI system and the corresponding PI consumption curve. **c** Liquid chromatogram and mass spectra of the eluate of the Fe/SCN after reaction. **d** The variation curves of intermediate products during 4-CP degradation. **e** The schematic diagram of the degradation mechanism of 4-CP by the Fe/SCN + PI system. **f** Degradation curves for different halophenols pollutants by the Fe/SCN + PI system (the error bars in **a**, **b** and **f** are all standard deviations calculated from the results of three parallel experiments).

small molecule products with good microbial degradability in the Fe/SCN + PI system facilitates further biochemical treatment of the actual organic wastewater. In addition, the Fe/SCN + PI system shows good degradation of different halophenols (Fig. 4f and Supplementary Fig. 23), presenting the universality of the contaminant-triggered ETP and $^1O_2$ synergistic degradation mechanism for halophenol degradation in this system.

Evaluation of practical application potential

The potential of the Fe/SCN for practical applications is verified. In Fig. 5a, b, the Fe/SCN + PI system shows excellent degradation performance for 4-CP over a wide pH range (pH = 2.5-10.5) and natural waters, which demonstrates that the Fe/SCN has superior environmental adaptability[50]. As shown in Fig. 5c, the degradation rate of 4-CP has no obvious decrease in five cycles. The texture of the Fe/SCN after cycling experiments remains unchanged and maintains the lamellar morphology, and the Fe is still atomically distributed without agglomeration (Supplementary Figs. 24–26). As demonstrated in Supplementary Fig. 27, the valence state of Fe have no obvious changed as the reaction proceeds, confirming that the ETP-dominated mechanism in the Fe/SCN + PI system avoids the redox cycling of the catalysts and thus maintains the efficient degradation performance in the cycling experiments. And the Fe *2p* spectra of the Fe/SCN have no obvious change before and after the reaction (Supplementary Fig. 28).

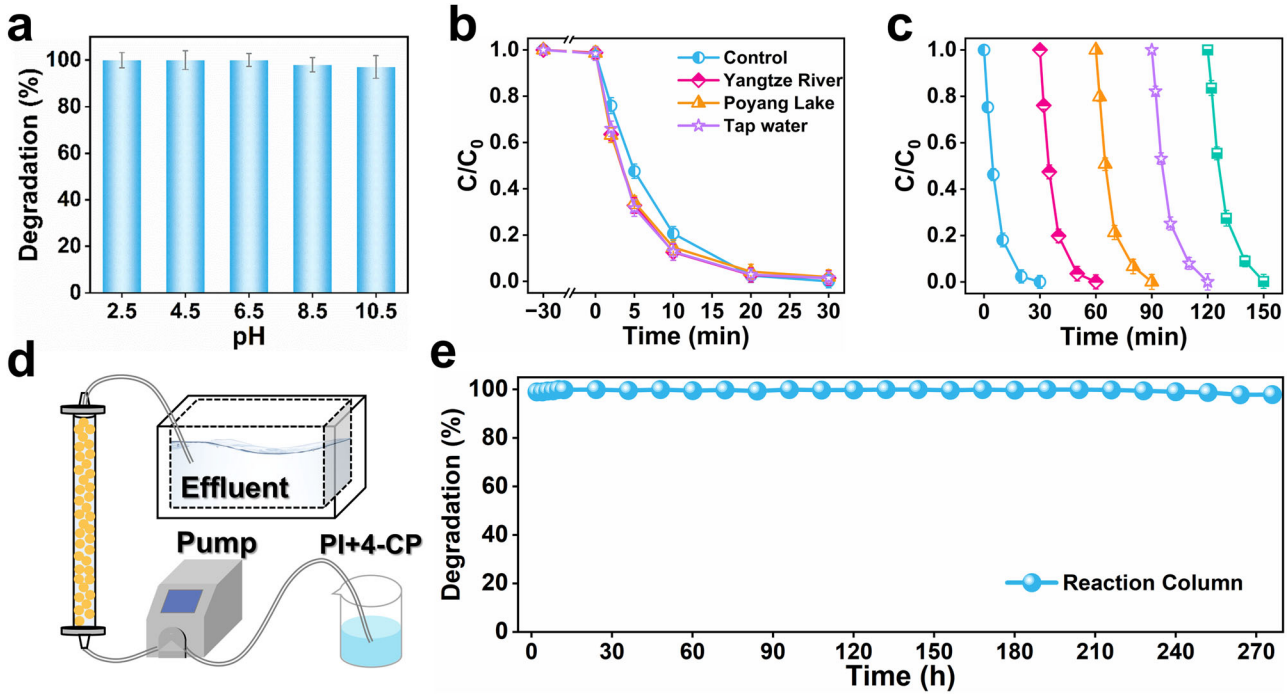

Fig. 5 | Evaluation of the adaptability and stability of the Fe/SCN + PI system. **a** Degradation efficiency of 4-CP under different pH in the Fe/SCN + PI system. **b**, **c** Degradation curves of 4-CP in different natural waters (**b**) and degradation curves of 4-CP for five catalytic cycles (**c**) in the Fe/SCN + PI system (the error bars in **a**–**c** are all standard deviations calculated from the results of three parallel experiments). **d** The diagram of the continuous-flow reactor. **e** 4-CP degradation performance for the continuous-flow reactor consisting of the Fe/SCN-filled column.

Furthermore, the leaching amount of Fe in the Fe/SCN is lower than that of the Fe/CN (Supplementary Fig. 29). All the above experimental results prove that the Fe/SCN has excellent reusability. When phenol is added to the Fe/SCN + PI system, no iodinated phenols such as 4-IP and 2-IP are detected (the rectangular box in Supplementary Fig. 30a), which can rule out the existence of HOI[51]. The IO_4^- is almost stoichiometrically converted to non-toxic IO_3^- during the reaction (Supplementary Fig. 30b). The I_2/I_3^- are also ruled out by starch colorimetry (Supplementary Fig. 30c)[52]. These results confirm that the Fe/SCN + PI system does not form the low-valence iodine species containing potential environmental risks. The exclusion of toxic byproducts is also consistent with the results of the E. coli culture experiments (Supplementary Fig. 31). To evaluate the persistent reactivity of the system, a continuous-flow reactor consisting of a catalyst-filled column was constructed (Fig. 5d and Supplementary Fig. 32). Continuous degradation of 4-CP is achieved by activating PI using the prepared Fe/SCN-sodium alginate gel spheres as column packing. As shown in Fig. 5e, the degradation rate of 4-CP can be maintained at nearly 100% during the continuous reaction up to 270 h, indicating that the Fe/SCN has favorable potential for practical application.

Discussion

In this work, the charge-confined Fe single-atom catalysts (Fe/SCN) with Fe-N_3S_1 configuration are successfully synthesized. The Fe/SCN + PI system shows efficient degradation of 4-CP by combining the ETP and $^1O_2$. DFT calculations verify that the co-adsorption of reactants and the charge-confined active sites enable the electrons conducted by the contaminants to be further utilized in the activation of PI to generate $^1O_2$. The 100% selective dechlorination of the ETP and the subsequent ring-opening of $^1O_2$ realize the transformation of contaminants into small-molecule biodegradable products without the generation of oligomers. In addition, the Fe/SCN not only exhibits a wide pH tolerance and good recyclability but also presents continuous degradation up to about 270 hours. This work achieves the activation of oxidants by the contaminant's electron in the ETP system via the charge-confined Fe/SCN, which provides a perspective on the design of single-atom catalysts.

Methods

Chemicals

All chemicals were used as received without further purification. The details of chemical reagents were provided in supplementary information.

Synthesis of Fe/SCN

Melamine (MA, 8 mmol) and Cyanuric acid (CA, 5.6 mmol) were dissolved into 100 mL and 105 mL of deionized water, respectively. $Fe(NO_3)_3{\cdot}9H_2O$ (1.2 mmol) and Oxalic acid (OA, 2.4 mmol) were dissolved in 45 mL of deionized water and then added into CA solution. Following 5 min stirring, the mixed solution was added gradually to MA solution and stirred consistently for 4 h. The precursor was obtained by filtration and dry at 60 °C overnight. Precursor (2.5 g) was mixed well with thiourea (0.5 g) and then put into a crucible and placed in a tube furnace, and then pyrolysed at 600 °C for 4 h under Ar atmosphere. After natural cooling, the Fe/SCN was obtained.

Synthesis of Fe/CN

The synthesis process of the Fe/CN was identical to that of the Fe/SCN except that the precursor powder was pyrolysed directly without the addition of thiourea.

Synthesis of SCN

The synthesis process of the SCN was identical to that of the Fe/SCN, except that $Fe(NO_3)_3{\cdot}9H_2O$ was not added.

Synthesis of CN

The synthesis process of the CN was identical to that of the Fe/CN, except that $Fe(NO_3)_3{\cdot}9H_2O$ was not added.

Sample characterizations

The powder XRD pattern was conducted on a Bruker D8 Advance, and the source uses a Cu-Kα line at 0.1541 nm in a 2θ range from 5° to 70° with a scan rate of 2° min^{-1}. The FT-IR spectra were performed using a VERTEX70 Fourier Transform Microscopic infrared spectrometer. Transmission electron microscopy (TEM) and EDX spectroscopy were performed on the Tecnai F20 at 200 kV. High-angle annular dark-field (HAADF) images were acquired with a JEM-ARM200F TEM/STEM with a spherical aberration corrector working at 300 kV. The content of Fe in as-prepared catalysts was examined by an ICP-AES (ICAP 7200). X-ray photoelectron spectroscopy (XPS) was performed using a VG Escalab 250 spectrometer with an Al anode (Al-Kα = 1486.7 eV) radiation source and peak positions were corrected by the C *1s* spectrum at 284.8 eV. Fe K-edge XAFS analyses were performed with Si(111) crystal monochromators at the BL14W Beamline at the Shanghai Synchrotron Radiation Facility (SSRF) (Shanghai, China). Before the analysis at the beamline, samples were placed into aluminum sample holders and sealed using Kapton tape film. The XAFS spectra were recorded at room temperature using a 4-channel Silicon Drift Detector (SDD) Bruker 5040. Fe K-edge EXAFS spectra were recorded in transmission/fluorescence mode. Negligible changes in the line-shape and peak position of Fe K-edge XANES spectra were observed between two scans taken for a specific sample. The XAFS spectra of these standard samples were recorded in transmission mode. The spectra were processed and analyzed by the software codes Athena. The Brunauer-Emmett-Teller (BET) specific surface area of obtained catalysts were performed on a BELSORP-MAX Automatic specific surface area analyzer. The free radicals (such as ·OH and $\cdot O_2^-$) and singlet oxygen ($^1O_2$) were recorded on EPR spectrometer (Bruker A300, Germany) with 60.0 mM of DMPO and TEMP as the spin-trapper agent, respectively.

Catalytic performance

The catalytic degradation experiments for the model pollutant 4-CP (0.1 mM) were carried out at pH = 6.0 and room temperature without special instructions. The 50 mL beaker was always placed on a magnetic stirrer with a constant stirring speed during the reaction. The catalyst (25 mg, 0.5 g·L^{-1}) was evenly dispersed in the 4-CP solution (49.5 mL, 0.1 mM). After continuous stirring for 30 min, PI (0.5 mL of 0.25 M) was added to start the degradation reaction. At fixed time intervals, 1 mL of the reaction solution was withdrawn and filtered using a filter fitted with a nylon membrane with a pore size of 0.22 μm to remove the catalyst, and after filtration, the obtained reaction solution was injected into a centrifuge tube containing 0.1 mL of methanol for subsequent testing. Scavenging experiments were carried out on ·OH, $\cdot O_2^-$, $^1O_2$, and e^- using TBA, p-BQ, FFA, and $K_2Cr_2O_7$, respectively, to determine the active species in the reaction system. The amount of each scavenger was determined as a molar ratio to the PI, where TBA: PI = 1000:1, p-BQ: PI = 20:1, FFA: PI = 50:1 and $K_2Cr_2O_7$: PI = 20:1. All solutions required for the experiments were prepared with ultrapure water. At least three parallel control groups were set up for each experiment to ensure the accuracy of the experimental data. The error bars in all plots in the manuscript are represented by the standard deviation (SD).

Analysis methods

Conditions for high-performance liquid-phase testing of organic pollutants, DMA probe experiments, detection of iodinated byproducts, electrochemical testing conditions, toxicity assessment - E.Coli culture experiments, and preparation of the Fe/SCN-sodium alginate gel spheres were described in the supplementary information. Details of DFT calculations were also included.

Reporting summary

Further information on research design is available in the Nature Portfolio Reporting Summary linked to this article.

Data availability

The data supporting the findings of the study are included in the main text and supplementary information files. Additional data are available from the corresponding author upon request.

References

1. Yu, F. B. et al. Rapid self-heating synthesis of Fe-based nanomaterial catalyst for advanced oxidation. *Nat. Commun.* **14**, 4975 (2023).
2. Zhao, J., Shang, C. & Yin, R. A high-radical-yield advanced oxidation process coupling Far-UVC radiation with chlorinated cyanurates for micropollutant degradation in water. *Environ. Sci. Technol.* **57**, 18867–18876 (2023).
3. Chen, M. et al. Sustainable and rapid water purification at the confined hydrogel interface. *Adv. Mater.* **36**, 2311416 (2024).
4. Zhu, Y. S. et al. Deformation of charge density activated by conductive carbon with the piezoelectric effect of tourmaline for highly promoting Fe^{3+}/Fe^{2+} cycle in Fenton-like process. *Appl. Catal. B-Environ.* **334**, 122824 (2023).
5. Wu, Q. Y., Yang, Z. W., Wang, Z. W. & Wang, W. L. Oxygen doping of cobalt-single-atom coordination enhances peroxymonosulfate activation and high-valent cobalt-oxo species formation. *Proc. Natl Acad. Sci. Usa.* **120**, e2219923120 (2023).
6. Wang, C. et al. Accelerating Fe(III)/Fe(II) redox cycling in heterogeneous electro-Fenton process via S/Cu-mediated electron donor-shuttle regime. *Appl. Catal. B-Environ.* **342**, 123457 (2024).
7. Wang, G., Li, B. & Zhang, Y. F. Ammonia-mediated iron cycle for oxidizing agent activation in advanced oxidation process. *Water Res.* **242**, 120295 (2023).
8. Li, Y. J. et al. Enhanced chalcopyrite-catalyzed heterogeneous Fenton oxidation of diclofenac by ABTS. *J. Hazard. Mater.* **463**, 132908 (2024).
9. Peng, Y. H. et al. Thermodynamic and kinetic behaviors of persulfate-based electron-transfer regime in carbocatalysis. *Environ. Sci. Technol.* **57**, 19012–19022 (2023).
10. Shao, S. T. et al. Rapid pollutant degradation by peroxymonosulfate via an unusual mediated-electron transfer pathway under spatial-confinement. *RSC Adv.* **12**, 5236 (2022).
11. Kong, T. et al. Electron transfer to direct oxidation of aqueous organics by perovskites. *Nano Res.* **16**, 6316–6325 (2023).
12. Yan, Y. Q. et al. Merits and limitations of radical vs. nonradical pathways in persulfate-based advanced oxidation processes. *Environ. Sci. Technol.* **57**, 12153–12179 (2023).
13. Liang, J. et al. pH-dependent generation of radical and nonradical species for sulfamethoxazole degradation in different carbon/persulfate systems. *Water Res.* **224**, 119113 (2022).
14. Dou, J. B. et al. Neglected but efficient electron utilization driven by biochar-coactivated phenols and peroxydisulfate: Polyphenol accumulation rather than mineralization. *Environ. Sci. Technol.* **57**, 5703–5713 (2023).
15. Zhang, Q. M. et al. Mineralization versus polymerization pathways in heterogeneous Fenton-like reactions. *Water Res.* **249**, 120931 (2024).
16. Luo, K. Y. et al. Activation of periodate by N-doped iron-based porous carbon for degradation of sulfisoxazole: Significance of catalyst-mediated electron transfer mechanism. *J. Hazard. Mater.* **457**, 131790 (2023).
17. Ren, W. et al. Electro-induced carbon nanotube discrete electrodes for sustainable persulfate activation. *Environ. Sci. Technol.* **56**, 14019–14029 (2022).
18. Yu, S. P. et al. Electron-transfer-based peroxymonosulfate activation on defect-rich carbon nanotubes: Understanding the substituent effect on the selective oxidation of phenols. *J. Hazard. Mater.* **442**, 130108 (2023).
19. Long, Y. K. et al. Atomically dispersed cobalt sites on graphene as efficient periodate activators for selective organic pollutant degradation. *Environ. Sci. Technol.* **55**, 5357–5370 (2021).

20. Qin, M. Z. et al. Reveals that electron transfer regime mediated by electron shuttle rather than adjacent transfer in B-doped 3D porous carbon framework: Exploration of interactions and identification of the main active site. *Appl. Catal. B-Environ.* **324**, 122285 (2023).
21. Ming, H. B. et al. Carbon nitride with a tailored electronic structure toward peroxymonosulfate activation: A direct electron transfer mechanism for organic pollutant degradation. *Appl. Catal. B-Environ.* **341**, 123314 (2024).
22. Li, J. et al. Achieving efficient incorporation of π-electrons into graphitic carbon nitride for markedly improved hydrogen generation. *Angew. Chem. Int. Ed.* **131**, 2007–2011 (2019).
23. Guo, Q. et al. Stitching electron localized heptazine units with "carbon patches" to regulate exciton dissociation behavior of carbon nitride for photocatalytic elimination of petroleum hydrocarbons. *Chem. Eng. J.* **452**, 139092 (2023).
24. Jiang, N., Lyu, L., Yu, G. F., Zhang, L. L. & Hu, C. A dual-reaction-center Fenton-like process on -C≡N-Cu linkage between copper oxides and defect-containing g-C_3N_4 for efficient removal of organic pollutants. *J. Mater. Chem. A* **6**, 17819 (2018).
25. Ming, H. B. et al. Tailored poly-heptazine units in carbon nitride for activating peroxymonosulfate to degrade organic contaminants with visible light. *Appl. Catal. B-Environ.* **311**, 121341 (2022).
26. Chen, Z. et al. Single-atom Mo-Co catalyst with low biotoxicity for sustainable degradation of high-ionization-potential organic pollutants. *Proc. Natl Acad. Sci. Usa.* **120**, e2305933120 (2023).
27. Li, Y. N. et al. Recent advance of atomically dispersed dual-metal sites carbocatalysts: Properties, synthetic materials, catalytic mechanisms, and applications in persulfate-based advanced oxidation process. *Adv. Funct. Mater.* **33**, 2301229 (2023).
28. Kong, X. J., Zhou, P. P. & Wang, Y. Chalcogen–π Bonding Catalysis. *Angew. Chem. Int. Ed.* **60**, 9395–9400 (2021).
29. Wang, W. et al. Chalcogen-chalcogen bonding catalysis enables assembly of discrete molecules. *J. Am. Chem. Soc.* **141**, 9175–9179 (2019).
30. Liao, W. X., Lyu, L., Wang, D., Hu, C. & Li, T. Graphitized Cu-β-cyclodextrin polymer driving an efficient dual-reaction-center Fenton-like process by utilizing electrons of pollutants for water purification. *J. Environ. Sci.* **126**, 565–574 (2023).
31. Zhang, L. S. et al. Carbon nitride supported high-loading Fe single-atom catalyst for activating of peroxymonosulfate to generate $^1O_2$ with 100% selectivity. *Angew. Chem. Int. Ed.* **60**, 1–6 (2021).
32. Jiang, X. H. et al. Silver single atom in carbon nitride catalyst for highly efficient photocatalytic hydrogen evolution. *Angew. Chem. Int. Ed.* **59**, 23112–23116 (2020).
33. Ling, C. et al. Sulfide-modified zero-valent iron activated periodate for sulfadiazine removal: Performance and dominant routine of reactive species production. *Water Res.* **220**, 118676 (2022).
34. Cui, J. H. et al. Robust Fe-N4 center with optimized metal-support interaction for efficient pollutant degradation by Fenton-like reaction. *Appl. Catal. B-Environ.* **331**, 122706 (2023).
35. Song, J. S. et al. Asymmetrically coordinated CoB_1N_3 moieties for selective generation of high-valence Co-Oxo species via coupled electron-proton transfer in Fenton-like reactions. *Adv. Mater.* **35**, 2209552 (2023).
36. Chen, S. Y. et al. Unveiling the proton-feeding effect in sulfur-doped Fe-N-C single-atom catalyst for enhanced CO_2 electroreduction. *Angew. Chem. Int. Ed.* **61**, e202206233 (2022).
37. Shao, C. F. et al. A versatile approach to boost oxygen reduction of Fe-N_4 sites by controllably incorporating sulfur functionality. *Adv. Funct. Mater.* **31**, 2100833 (2021).
38. Guo, Y. P. et al. Sulfur-doped activated carbon for the efficient degradation of tetracycline with persulfate: Insight into the effect of pore structure on catalytic performance. *RSC Adv.* **14**, 11470–11481 (2024).
39. Tian, L. et al. Overcoming electrostatic interaction via strong complexation for highly selective reduction of CN^- into N_2. *Angew. Chem. Int. Ed.* **61**, e202214145 (2022).
40. Tian, L. et al. Efficient homolytic cleavage of H_2O_2 on hydroxyl-enriched spinel $CuFe_2O_4$ with dual lewis acid sites. *Angew. Chem. Int. Ed.* **63**, e202401434 (2024).
41. Luo, M. F. et al. Insights into the role of in-situ and ex-situ hydrogen peroxide for enhanced ferrate(VI) towards oxidation of organic contaminants. *Water Res.* **203**, 117548 (2021).
42. Zong, Y. et al. Surface-mediated periodate activation by nano zero-valent iron for the enhanced abatement of organic contaminants. *J. Hazard. Mater.* **423**, 126991 (2022).
43. Ren, W. et al. Origins of electron-transfer regime in persulfate-based nonradical oxidation processes. *Environ. Sci. Technol.* **56**, 78–97 (2022).
44. Yun, E. T., Yoo, H. Y., Bae, H., Kim, H. I. & Lee, J. Exploring the role of persulfate in the activation process: Radical precursor versus electron acceptor. *Environ. Sci. Technol.* **51**, 10090–10099 (2017).
45. Wang, M. M. et al. Multimetallic CuCoNi oxide nanowires in situ grown on a nickel foam substrate catalyze persulfate activation via mediating electron transfer. *Environ. Sci. Technol.* **56**, 12613–12624 (2022).
46. Zhu, C. Q. et al. Constructing surface micro-electric fields on hollow single-atom cobalt catalyst for ultrafast and anti-interference advanced oxidation. *Appl. Catal. B-Environ.* **305**, 121057 (2022).
47. Xu, Z. M., Wang, J., Qiu, J. K., Cao, H. B. & Xie, Y. B. Unexpectedly enhanced organics removal in persulfate oxidation with high concentration of sulfate: The origin and the selectivity. *Environ. Sci. Technol.* **57**, 14442–14451 (2023).
48. Xie, L. B. et al. Pauling-type adsorption of O_2 induced electrocatalytic singlet oxygen production on N-CuO for organic pollutants degradation. *Nat. Commun.* **13**, 5560 (2022).
49. Wang, L. J., Xiao, K. & Zhao, H. Z. The debatable role of singlet oxygen in persulfate-based advanced oxidation processes. *Water Res.* **235**, 119925 (2023).
50. Lan, M. Y. et al. Multi-channel electron transfer induced by polyvanadate in metal-organic framework for boosted peroxymonosulfate activation. *Nat. Commun.* **15**, 7208 (2024).
51. Li, D. F. N. et al. Ru(III)-periodate for high performance and selective degradation of aqueous organic pollutants: Important role of Ru(V) and Ru(IV). *Environ. Sci. Technol.* **57**, 12094–12104 (2023).
52. Zong, Y. et al. Enhanced oxidation of organic contaminants by iron(II)-activated periodate: The significance of high-valent iron–oxo species. *Environ. Sci. Technol.* **55**, 7634–7642 (2021).

Acknowledgements

We gratefully acknowledge the financial support of the National Natural Science Foundation of China (52100186, L.Z. 52170082, J.Z. and 51938007, J.Z.), the Natural Science Foundation of Jiangxi Province (20225BCJ23003, L.Z. 20212ACB203008, J.Z. and 20223AEI91001, J.Z.), and the support by Key Laboratory of Jiangxi Province for Persistent Pollutants Prevention Control and Resource Reuse (No. 2023SSY02061, J.Z.).

Author contributions

L.Z. T.M. and J.Z. conceived the ideas and co-wrote the manuscript. J.Z. supervised the entire project. Q.T., B.W., X.H., W.R. and Y.C. prepared, characterized, and tested the catalysts. L.Z., Q.T., L.L. and L.T. analyzed the data. Q.S. and Z.K. designed and performed the DFT calculations. All the authors participated in the discussion of the results and manuscript preparation and revision.

Competing interests
The authors declare no competing interests.

Additional information
Supplementary information The online version contains supplementary material available at https://doi.org/10.1038/s41467-024-53941-8.

Correspondence and requests for materials should be addressed to Long-Shuai Zhang or Jian-Ping Zou.

Peer review information *Nature Communications* thanks Ivo F. Teixeira, Chong-Chen Wang and the other, anonymous, reviewers for their contribution to the peer review of this work. A peer review file is available.